Aeroacoustics noise prediction for the airfoil-rod benchmark using high-order large eddy simulation on unstructured grids and the acoustic analogy approach in frequency-domain

R. B. Modi*, M. A. Alhawwary †, A. M. Akbarzadeh†, F. D. Witherden‡, and A. Jameson §
Texas A& M University, College Station, TX, 77843

An implicit large eddy simulation (ILES) is coupled with a frequency-domain Ffowcs Williams-Hawkings (FWH) acoustic analogy formulations for the noise prediction of the airfoil-rod problem. Higher order Flux-Reconstruction method is used for spatial discretisation. The airfoil-rod case is simulated based on the compressible Navier-Stokes equations for a relatively high Reynolds number (Re = 480,000) and a Mach number of (M = 0.2) in accordance with the experimental setup. The FWH acoustic analogy solver is implemented in the open-source massively parallel software PyFR which is a Python based computational fluid dynamics (CFD) solver developed for heterogeneous computing systems. The main goal of this work is to investigate the use of high-order methods on unstructured grids for such acoustic problems and assess the suitability of the hybrid approach in computational aeroacoustics with high-order discretization methods. The near-field aerodynamics based on averaged pressure and friction coefficients is computed and validated before the farfield acoustics are collected and results show good agreement with experimental and numerical literature.

I. Introduction

The industrial goals for green aviation set forth by many governmental agencies has also led to considerable interest in reducing other environmental aspects of the airplane industry such as airframe, landing-gear and jet noise. These types of noise problems impact both military and civil personnel either on aircraft carriers or in modern cities where airports are often built close to high population density areas. Thus accurate and affordable noise predictions for these problems has gained considerable interest in the computational fluid dynamics (CFD) and acoustic communities.

Several approaches exist for sound propagation in a fluid medium, among which the hybrid large eddy simulation (LES)-acoustic analogy approach stands as a more practical methodology. The hybrid approach for aeroacoustics predictions consists of solving the Navier-Stokes equations to determine the near-field turbulent flow characteristics and then utilize these data with the acoustic analogy equations for farfield noise predictions. For the noise generated by turbulent flows, accurate acoustic propagation depends on the quality of the near-field results. In this regard, LES offers an efficient and affordable simulation model for resolving the energy-bearing eddies and modeling the dissipative scales. This hybrid approach has been employed by several researches for jet noise predictions [1–5] as well as other turbulent flow-based noise predictions [6–9]. The desired ingredients for an efficient numerical discretization methods for LES are high accuracy and the ability to work with unstructured grids. For this purpose we utilize the high-order flux reconstruction (FR) method, first introduced by [10] and further extended by Wang et. al [11] for hybrid unstructured meshes. In the context of LES, high-order methods such as FR have been shown to be less dissipative than the classical FD and CD schemes [12, 13] when employed in an implicit large eddy simulation (ILES) approach [14–16] where no sub-grid scale (SGS) model is used. Thus these methods are more suitable for highly separated flows and vortex propagation problems. In addition, these methods can work routinely with mixed unstructured grids which is needed for complex geometries involved in airplane noise problems.

To validate this hybrid approach for more complex airframe and landing-gear noise problems the airfoil-rod problem has been used by many researchers [6, 17–21] as a benchmark case since first introduced by Jacob et. al [22] experiment. Indeed, this problem contains many of the interesting noise features encountered in a landing-gear problem such as the quasi-tonal noise caused by the vortex shedding of the rod and broadband noise spectrum due to impingement

*PhD student, Department of Ocean Engineering, Haynes Engineering Building, 727 Ross St
†Postdoctoral Researcher, Department of Aerospace engineering, 701 H.R. Bright Building 3141
‡Assistant Professor, Department of Ocean engineering, Haynes Engineering Building, 727 Ross St
§Professor, Department of Aerospace engineering, 701 H.R. Bright Building 3141

of the rod wake on the airfoil surface. This provides a well represented case with availability of experimental and numerical data for validating noise generated by bluff bodies in a highly separated turbulent flow [23]. This consists of a turbulent flow simulation over a rod placed 1.05C (C: chord length) in front of NACA0012 airfoil at 0° angle of attack at $Re = 480,000$ and $M = 0.2$.

In this work, we equipped the high-order cross-platform solver PyFR [24] with a Ffowcs Williams Hawkings (FWH) solver both implemented in Python for the simulation of the rod-airfoil turbulent flow based noise predicition problem. This paper is organized as follows. Section II is dedicated for introducing the numerical models where both the flow and acoustic solvers are discussed. We then present the problem setup in Section III and the numerical results in Section IV.

II. Methodology

A. The PyFR flow solver and the FR method

The flow model is based on the compressible Navier-Stokes equations which can be written in a conservative form as follows

$$\frac{\partial \mathbf{u}}{\partial t} + \boldsymbol{\nabla} \cdot \mathbf{f} = 0, \tag{1}$$

where $\mathbf{u} = \mathbf{u}(\mathbf{x}, t) = (\rho, \rho v_x, \rho v_y, \rho v_z, E)$, is the solution, ρ is the density, $\mathbf{v} = (v_x, v_y, v_z)$ are the fluid velocity components in x, y, z directions, respectively, and E is the total energy per volume of the fluid. Here, $\mathbf{f} = \mathbf{f}(\mathbf{u}, \boldsymbol{\nabla}\mathbf{u}) = \mathbf{f}^i - \mathbf{f}^v$ is the flux with $\mathbf{f}^i$ the inviscid flux given by

$$\mathbf{f}^i = \begin{pmatrix} \rho v_x & \rho v_y & \rho v_z \\ \rho {v_x}^2 + p & \rho v_x v_y & \rho v_x v_z \\ \rho v_x v_y & \rho {v_y}^2 + p & \rho v_y v_z \\ \rho v_x v_z & \rho v_y v_z & \rho {v_z}^2 + p \\ v_x(E+p) & v_x(E+p) & v_z(E+p) \end{pmatrix}, \tag{2}$$

where p is the pressure which is for an ideal gas is

$$p = (\gamma - 1)(E - \frac{1}{2}\rho||\mathbf{v}||^2), \tag{3}$$

where $\gamma = c_p/c_v$, where c_p and c_v are specific heat capacities at constant pressure and volume, respectively. The viscous flux is

$$\mathbf{f}^v = \begin{pmatrix} 0 & 0 & 0 \\ \tau_{xx} & \tau_{yx} & \tau_{zx} \\ \tau_{xy} & \tau_{yy} & \tau_{zy} \\ \tau_{xz} & \tau_{yz} & \tau_{zz} \\ v_l \tau_{lx} + \Delta \partial_x T & v_l \tau_{ly} + \Delta \partial_y T & v_l \tau_{lz} + \Delta \partial_z T \end{pmatrix}. \tag{4}$$

In the above we have defined $\Delta = \mu c_p/Pr$ where μ is the dynamic viscosity and Pr is the Prandtl number. The components of the stress–energy tensor are given by

$$\tau_{lm} = \mu(\partial_l v_m + \partial_m v_l) - \frac{2}{3}\mu \delta_{lm} \boldsymbol{\nabla} \cdot \mathbf{v}, \tag{5}$$

Using the ideal gas law, the temperature is

$$T = \frac{1}{c_v} \frac{1}{\gamma - 1} \frac{p}{\rho}. \tag{6}$$

The fluid properties employed in this work are $\gamma = 1.4$ and $Pr = 0.71$, and flow Mach number is $M = 0.2$.

In this study, the compressible Navier-Stokes Equations are solved with a multidimensional Flux reconstruction (FR) approach for space discretization implemented in PyFR. PyFR is an open-source software that can solve the compressible Navier–Stokes equations on mixed unstructured grids and is designed to target a range of modern hardware platforms, including heterogeneous mixtures of CPUs and GPUs, via C/OpenMP, CUDA, HIP and OpenCL backends [24, 25]. The FR approach introduced by Huynh [10] is a nodal numerical formulations for solving hyperbolic partial differential equations. The method has been further developed by several groups [26–28] for advection-diffusion problems and extended to mixed unstructured grids [25, 29]. In addition, high-order FR method has proved successful for a number of large eddy simulations based on the implicit approach [14] as shown in [15, 30–32] and more recently based on the Partially Averaged Navier-Stokes equations (PANS) in Dzanic et. al [33].

In the FR method, the domain Ω is partitioned into N_e non overlapping elements Ω_e such that $\bigcup_{i=1}^{N_e} \Omega_e = \Omega$. Considering equation 1, the solution vector takes the form

$$\mathbf{u} = \sum_{i=1}^{N_p} \mathbf{u_i} \phi_\mathbf{i} \tag{7}$$

inside each element Ω_e. Here, N_p is the number of solution points inside the element and ϕ is the set of nodal basis functions. A discontinuous approximation of the flux is obtained by taking a collocation projection of the flux function on the solution nodes and is defined as

$$\mathbf{f}^D = \sum_{i=1}^{N_p} \mathbf{f_i^D} \phi_\mathbf{i} \tag{8}$$

where $\mathbf{f_i^D}$ is the value of the flux at solution points. To allow for data interaction between adjacent cells in flux reconstruction, the discontinuous flux $\mathbf{f}^D$ is corrected by adding a correction flux polynomial. After adding the correction, the flux function takes the form

$$\mathbf{f}^C = \mathbf{f}^D + \sum_{i=1}^{N_f} \left[\mathbf{f}_i^I - \mathbf{f}_i^D \cdot \mathbf{n}_i \right] \mathbf{h}_i \tag{9}$$

where $\mathbf{f}^i$ is the interface flux, N_f is the number of flux points, $\mathbf{n}_i$ their normals and $\mathbf{h}_i$ is the correction function, which belongs to the Raviart–Thomas space. The corrected flux $\mathbf{f}^C$ can now be differentiated to obtain the divergence of flux. For more details on the FR method, interested readers can consult the following reviews [34, 35]. In the present work, a Rusanov Riemann solver utilising the Davis wave speed [36] is used to calculate the inter-element inviscid fluxes, the local discontinuous Galerkin [37] approach is used to calculate the inter-element viscous fluxes, an adaptive time-step Runge–Kutta (RK45) scheme [38] is utilized to advance the solution in time.

B. The FWH solver

The *permeable/porous* surface FWH equations [39, 40] based on the moving medium formulation [41, 42], can be written using index summation notation as,

$$\Box^2 \left[H(f)\, p'(x,t) \right] = \frac{\partial}{\partial t} \left[Q\delta(f) \right] - \frac{\partial}{\partial x_l} \left[L_l \delta(f) \right] + \frac{\partial^2 (H(f) T_{lm})}{\partial x_l \partial x_m}, \tag{10}$$

where $\Box^2 = \frac{1}{c^2}\frac{D^2}{Dt^2} - \frac{\partial^2}{\partial x_i \partial x_i}$ is the d'Alembert wave operator and

$$\begin{aligned} T_{lm} &= \rho u_l u_m + \left[(p - p_o) - c^2(\rho - \rho_o) \right] \delta_{lm} - \sigma_{lm}, \\ L_l &= \rho u_l \left[u_n - (v_n - U_{\infty n}) \right] + \left[(p - p_o)\delta_{lm} - \sigma_{lm} \right] \hat{n}_m, \\ Q &= \rho \left[u_n - (v_n - U_{\infty n}) \right] + \rho_o (v_n - U_{\infty n}), \end{aligned} \tag{11}$$

The description of the above symbols is as follows. On the left hand side of Eq. (10), $p' = p - p_o$ is the acoustic perturbation pressure. For small disturbances $\rho'/\rho_o \ll 1$, the pressure disturbance/acoustic pressure $p' = c^2\rho' = c^2(\rho - \rho_o)$ which is valid for the left hand side of the equation that is evaluated at an observer distance far away from the surface where the flow can be assumed isentropic. The symbols p_o, ρ_o are the pressure and density of the undisturbed flow and c is the speed of sound, i.e., free stream values. $H(f)$ is the Heaviside function which is defined as

$$H(f(\mathbf{x},t)) = \begin{cases} 1: & f(\mathbf{x},t) > 0 \\ 0: & f(\mathbf{x},t) < 0 \end{cases} \tag{12}$$

and $\delta(f)$ is the dirac delta function defined as

$$\delta(f(\mathbf{x},t)) = \frac{\partial H}{\partial f} = \begin{cases} 1: & f(\mathbf{x},t) = 0 \\ 0: & f(\mathbf{x},t) \neq 0 \end{cases} \tag{13}$$

and $f(\mathbf{x},t)$ is the data surface equation as shown in Fig. 1a.

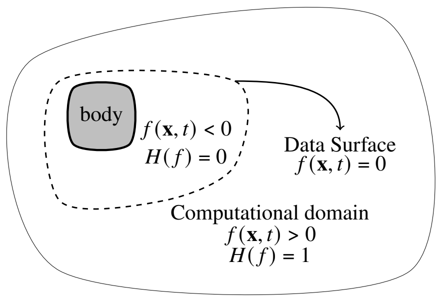

(a) Computational Domain

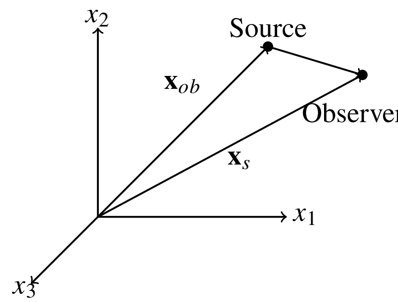

(b) Frames of reference

Fig. 1 Acoustics model

Thus, in the right hand side of Eq. (10), the first two terms represents a surface dipole and monopole sources defined only on the data surface and the last term is a volume quadrupole term defined in the exterior flow domain where $f(\mathbf{x},t) > 0$. In Eq. (11), σ_{lm} is the viscous stress tensor, u_l is the perturbed fluid velocity such that $u_l = u_l - U_\infty$ and v_l is the surface velocity assuming a fixed frame of reference x. The Lighthill's equivalent stress tensor is represented by T_{lm}. This completes the presentation of the FWH equation for a stationery observer or fly-over problems. In the current implementation we neglect the volume source T_{lm} as well as the viscous stresses effects σ_{lm}. In this formulation Eq. (10), the problem of an observer moving to the left of a fixed frame $\mathbf{x}'$ in a medium at rest is transformed into a fixed observer but in a flow blowing to the right, positive $\mathbf{x}'$-direction, with constant and uniform velocity U_∞ and a moving data surface with relative velocity $v - U_\infty$ to the free stream, see Fig. 1b. Note that for a solid FWH surface, Eq. (10) still applies with $u_n = v_n - U_{\infty n}$ to satisfy the impermeability condition.

For solving the above equation an integral formulation is often used based on the free-space Green function, see for example [40, 42–45]. For a surface moving in a medium at rest with uniform and constant velocity, equivalent to a stationery source in a wind tunnel case, an efficient frequency-domain formulation was proposed by Lockard [41] and a generalization by [46]. First, the free space Green function in frequency domain can be written as

$$G(\boldsymbol{x},t;\boldsymbol{y},\tau) = \frac{1}{2\pi}\int_\omega \frac{e^{-j\kappa R}}{4\pi R^*} e^{j\omega(t-\tau)} d\omega, \tag{14}$$

where $\kappa = \omega/c$ is the acoustic wavenumber, ω is the angular frequency and $j = \sqrt{-1}$. The radial distance variables R, R^* are defined as

$$R^* = \frac{r}{\beta}\sqrt{1+\beta^2 M_{\infty r}^2}, \quad R = \beta^2\left(R^* - rM_{\infty r}\right). \tag{15}$$

where, $r = |\mathbf{x} - \mathbf{y}(\tau)|$ is the distance between the source position $\mathbf{x}_s$ and the observer position $\mathbf{x}_{ob}$, see 1b. In addition, $M_{\infty r} = M_{\infty l}\hat{r}_l, \hat{r}_l = r_l/r$ and $\beta = 1/\sqrt{1-|M_\infty|^2}$ is the reciprocal of the Prandtl-Glauret correction factor. The frequency-domain formulation starts by performing a Fourier transformation of equation Eq. (10) followed by utilizing the Green function for integration and convolution to end up with the following components of acoustic pressure

$$
\begin{aligned}
4\pi \tilde{p}_1(\boldsymbol{x},\omega) &= \int\limits_{f=0} \left[\frac{j\omega\tilde{Q}(\boldsymbol{\xi},\omega)}{R^*}\right] e^{-j\kappa R} dS, \\
4\pi \tilde{p}_2(\boldsymbol{x},\omega) &= \int\limits_{f=0} \left[\frac{j\,\kappa\,\tilde{F}_R(\boldsymbol{\xi},\omega)}{R^*} + \frac{\tilde{F}_{R^*}(\boldsymbol{\xi},\omega)}{R^{*2}}\right] e^{-j\kappa R} dS,
\end{aligned}
\tag{16}
$$

where $\tilde{F}_R = \tilde{F}_l \hat{R}_l$, $\tilde{F}_{R^*} = \tilde{F}_l \hat{R}^*_l$. The quantities with $\tilde{Q}, \tilde{F}_l$ are the Fourier transformed quantities of Q, F_l where $F_l = L_l - QU_{\infty l}$. The distance quantities $\hat{R}_m, \hat{R}^*_m$ are given by

$$
\begin{aligned}
\hat{R}^*_l &= \frac{\partial R^*}{\partial x_l} = \frac{r}{\gamma^2 R^*}\left(\hat{r}_l + \gamma^2 M_{\infty r} M_{\infty l}\right), \\
\hat{R}_l &= \frac{\partial R}{\partial x_l} = \frac{r}{R^*}\left(\hat{r}_l + \gamma^2 M_{\infty r} M_{\infty l}\right) - \gamma^2 M_{\infty l}.
\end{aligned}
\tag{17}
$$

Finally, the acoustic pressure in the frequency-domain can be computed as

$$
\tilde{p}(\boldsymbol{x},\omega) = \tilde{p}_1(\boldsymbol{x},\omega) + \tilde{p}_2(\boldsymbol{x},\omega). \tag{18}
$$

The implementation of this methodology in combination with the high-order method in PyFR follows the same approach as presented in [47]. This implementation features a streaming algorithm for computing the spectral data at the far-field in an online manner as the flow simulation marches in time. PyFR routinely works with unstructured grids and the extraction of the acoustic data surface is made based on actual face elements. The surface integration is done efficiently for each surface element using the flux points on each face element since they are naturally of Gauss quadrature type. In PyFR the FWH solver is implemented as an acoustic analogy plugin feature which can be further extended to other types of acoustic analogies in an efficient manner.

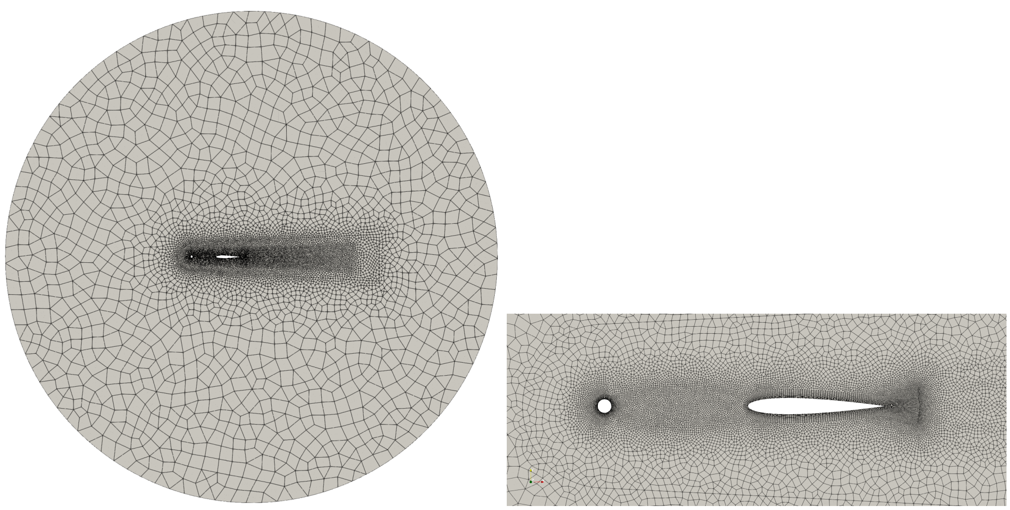

(a) Full mesh (b) Zoomed view

Fig. 2 Computational mesh

III. Problem Setup

The rod-airfoil case setup follows the setup of the experiment carried out by Jacob et. al [22] and the numerical simulations in the literature [17, 20, 21, 23, 48]. In this case, a rod with a diameter $d = 0.1$C is used and its center is placed at a distance of 1.05 C in front of a NACA0012 airfoil at zero angle of attack, where C is the airfoil chord length. The Reynolds number is $480,000$ based on airfoil chord and a Mach number M of 0.2 is used. The computational domain consists of a 2D unstructured mesh extruded to a $0.35C$ length in the spanwise (z-direction).

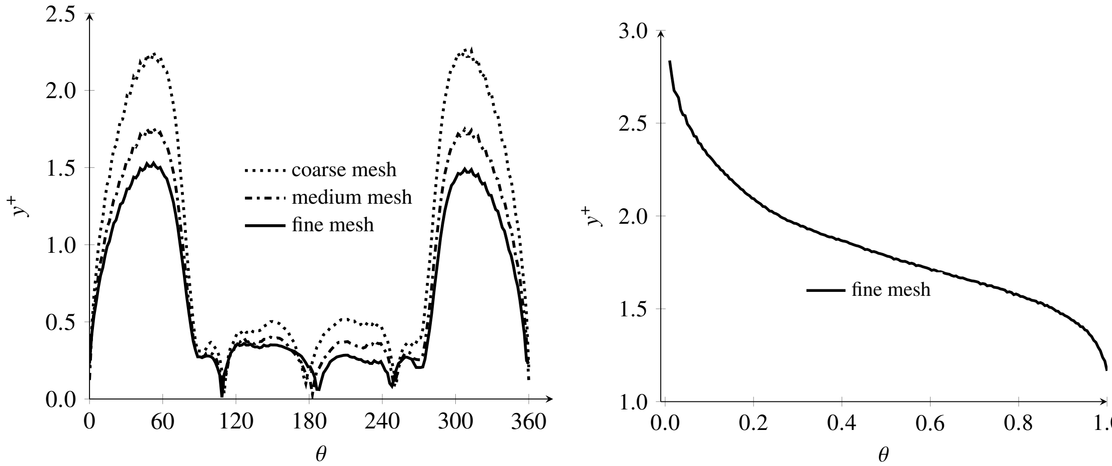

(a) Y^+ over the rod

(b) Y^+ over the airfoil

Fig. 3 Y$^+$ distribution.

The simulations are carried out on three different computational meshes (coarse, medium and fine) with refinement primarily in the boundary layer region of the rod. The fine computational mesh shown in Fig. 2 has 14 elements in the spanwise direction and $\sim 28 \times 10^3$ elements in the XY plane, bringing the total to $\sim 400 \times 10^3$ elements. The mesh has a structured boundary layer region around both the airfoil and the cylinder with wall heights of $1.25 \times 10^{-4} \cdot C$ and $3 \times 10^{-4} \cdot C$ for the rod and airfoil surfaces, respectively. Mesh is also refined in a near field region that contains the airfoil and rod and extends to the wake up to $6C \sim 7C$ for accurate representation of the turbulent wake. This refinement region is planned to be used for a study of the location of the porous FWH data surface providing the best results. The outer circle (farfield boundary) has a radius of approximately $10.5C$ and is centered at 1.5C distance downstream of the airfoil. The mesh has both prism and hexahedral element types. Polynomial order 3 is used to carry out the simulations, bringing the total number of degrees of freedom to 21 million. Fig. 3 shows the y^+ for the first solution node around the rod and airfoil. No refinement is done in the boundary layer region of the airfoil for the three meshes. The y^+ is obtained by dividing the actual cell height by $p + 1$, where p is the polynomial order. Characteristic Reimann invariants was used as a farfield boundary condition to minimize wave reflections and a no-slip adiabatic wall condition was used at rod and airfoil surface.

IV. Numerical Results

A parallel numerical simulation on a multi-GPU architecture is conducted using PyFR in an ILES approach without SGS model. Statistics are accumulated every 500 time steps. During the startup phase, simulations were run with polynomial order $p = 2$ for a time period of $96C/U_\infty$ after which simulations were run with $p = 3$ which is 4^{th} order accurate in space. Averaged statistics collection was started after a time period of $115C/U_\infty$ was completed. All the statistics presented in the paper are averaged for a time period of $70C/U_\infty$, equivalent to 70 passes over the airfoil.

Table 1 Mean and RMS drag coefficients for the rod.

Cases	$\langle C_d \rangle$	C_d'
PyFR fine mesh	1.23	0.145
PyFR medium mesh	1.22	0.14
PyFR coarse mesh	1.20	0.15
Giret et. al [20]	1.19	0.12

A. Turbulent flow and aerodynamic coefficients results

The mean and root mean square (RMS) of the drag coefficient for the three meshes are presented in Table 1. All the meshes agree within 4% of the literature values. The comparison of the mean and RMS pressure coefficient over the airfoil is shown in Fig. 4. For the average $\langle C_p \rangle$, comparison is made between Giret's LES data [20] and Jacob's experimental data [22]. There is hardly any difference between the LES data of Giret et al. and PyFR results. The error between the numerical results and experiment is observed consistently and can be due to the curvature discontinuity in the mockup leading-edge region as mentioned in [20]. The RMS value of the pressure coefficient over the airfoil matches well with Giret's LES data upto $x/c = 0.04$.

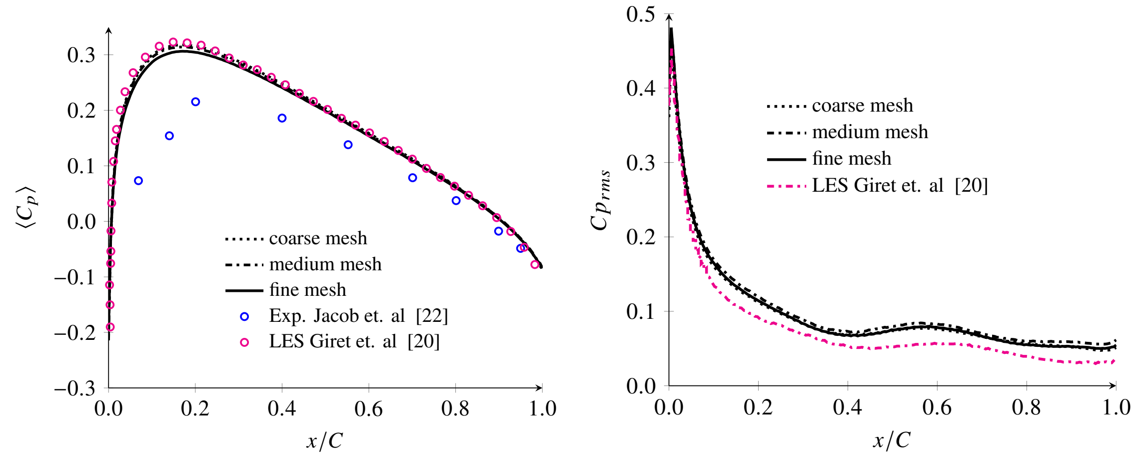

(a) Mean pressure coefficient on airfoil

(b) RMS pressure coefficient on airfoil

Fig. 4 Average and root mean square of the pressure coefficient over the airfoil surface.

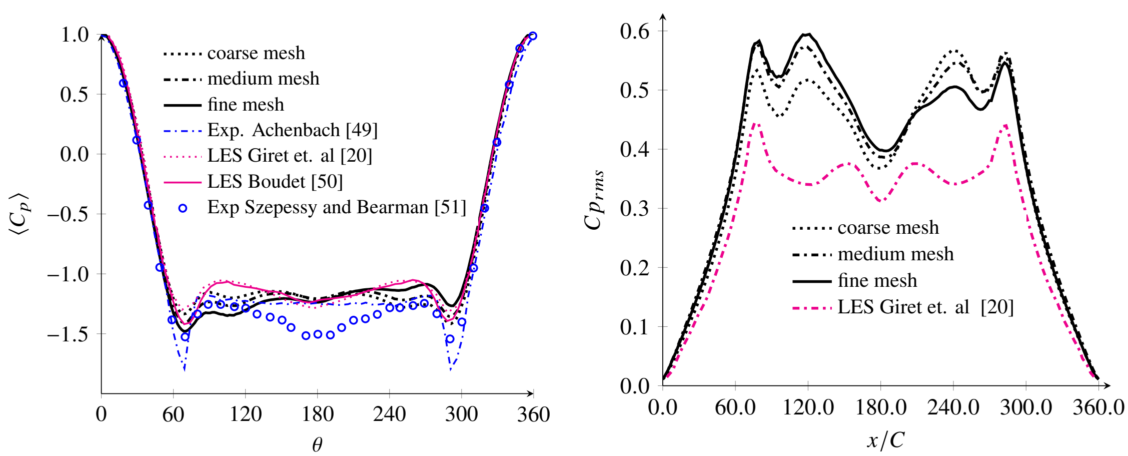

(a) Mean pressure coefficient on rod

(b) RMS pressure coefficient on rod

Fig. 5 Average and root mean square of the pressure coefficient over the rod surface.

Fig. 5 shows the comparison of mean and RMS pressure coefficient over the rod. For the average value of $\langle C_p \rangle$, data obtained from PyFR is compared with Giret's LES data, the LES of Boudet [50], and experiments of Szepessy and Bearman [51] and Achenbach [49]. The minimum value of average $\langle C_p \rangle$ is obtained at an angle of 70° starting from the rod upstream stagnation point, which matches well with the experiment of Szepessy and Bearman [51]. There is asymmetry in the average and RMS pressure coefficients of the rod, especially for the fine mesh, which can be attributed to lack of time averaging. Due to limitation in the resources, it was decided to rely on these results for the acoustics predictions in the meantime. Additionally, the discrepancy between PyFR LES results and experiments for average $\langle C_p \rangle$ can be attributed to the fact that the experiments were carried out for an isolated rod at a different Reynolds number. For the experiment by Szepessy and Bearman [51], the Reynolds number is 4×10^5, while it is 10^5 for the experiment by Achenbach [49]. As noted by Boudet [50], there is some upstream influence of the airfoil on the rod.

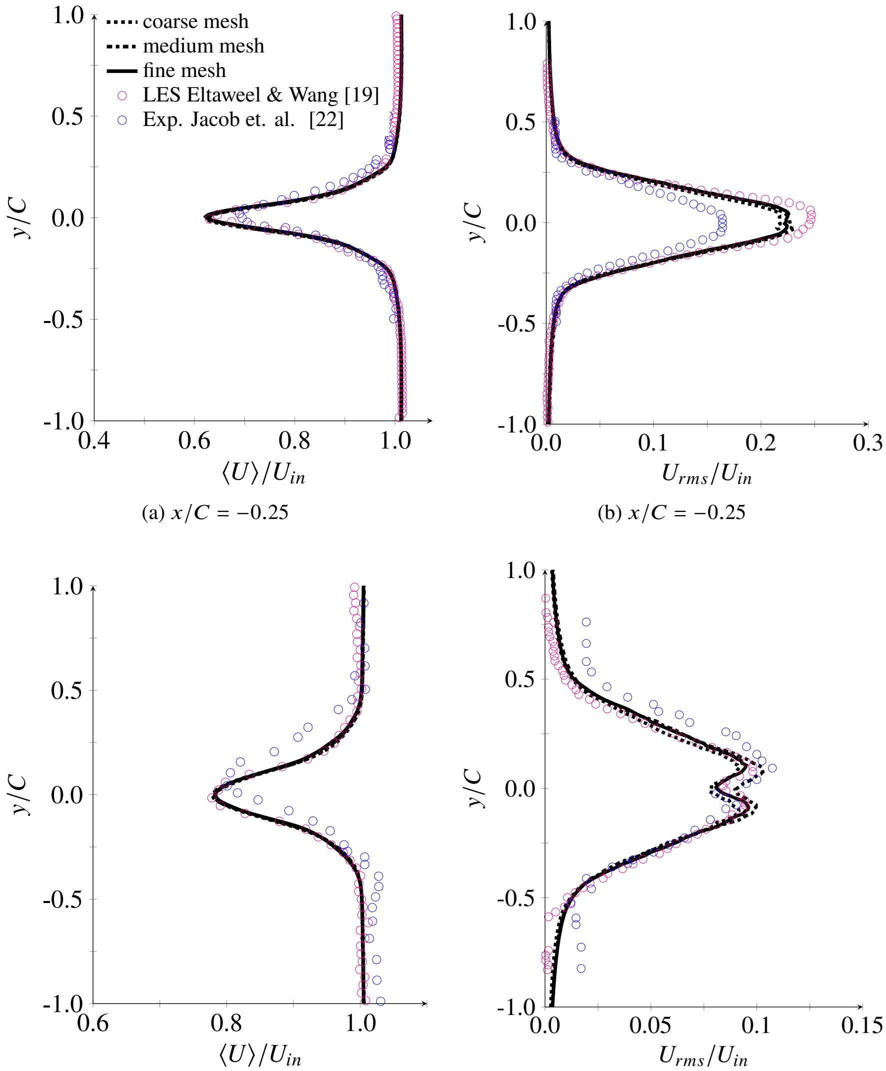

(a) $x/C = -0.25$ (b) $x/C = -0.25$

(c) $x/C = 2$ (d) $x/C = 2$

Fig. 6 Comparison of the mean and RMS velocity profiles with experiment and reference LES in the wake of cylinder and airfoil. Origin at airfoil Leading Edge.

Figure Fig. 6 shows the average values of the x-velocity (U) and RMS value of the x-velocity fluctuations (U_{rms}) at two different locations, viz., wake of the rod and wake of the airfoil. The numerical results obtained from PyFR P3 simulations match well with both the LES data of Eltaweel and Wang [19] and Jacob's experiment [22]. For the airfoil wake, the experimental dip in U occurs at a different y-location compared to the LES results. This can be explained by the misalignment in the rod and airfoil axis as mentioned by Jacob et. al. [22]. Otherwise, the U variation matches quite well with both the experiments and LES data. Values of U_{rms} matches well with the LES data. In the rod wake, the peak value of U_{rms}. is overpredicted by PyFR compared to experiments. However, the values are quite close to the LES data of Eltaweel and Wang. The peak value of U_{rms} is overpredicted by PyFR compared to experiments. However, the values are quite close to the LES data of Eltaweel and Wang. The difference in U and U_{rms} values between three different meshes on PyFR is negligible.

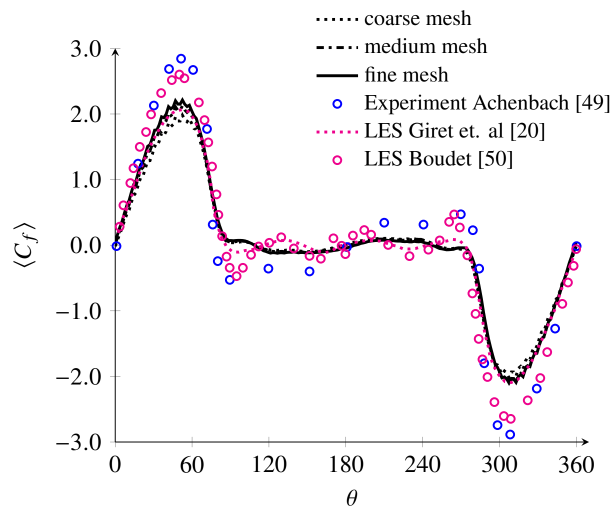

Fig. 7 Comparison of the mean skin friction $\langle C_f \rangle$ coefficient.

Figure Fig. 7 represents the skin friction coefficient over the surface of the rod. Skin friction coefficient C_f becomes zero at an angle of 107° from the upstream stagnation point indicating separation. Although the location of separation point does not match with literature values of 86° [49][50], it is worth noting that both Achenbach's experimental ($Re = 10^5$) results [49] and LES results of Boudet [50] are based on an isolated rod. The maximum C_f upstream of the separation point matches well with Giret et. al's LES data [20]. All three meshes with PyFR predict the same location of separation point.

B. The Farfield acoustics results

The FWH results are computed for an averaging time period of $34C/U_\infty$. The FWH follows the Welch's method of periodiograms [52] where the time period is divided into 6 windows each with length of $9.6C/U_\infty$ s. Strouhal number St for the problem based on literature is determined to be 0.19, bringing the period to be $0.5C/U_\infty$ s. Hence, the window length of $9.6C/U_\infty$ s should be sufficient to capture the acoustics. The farfield acoustics are computed for each period and averaged with the others with a 50% shift in time or window length. The acoustic results are presented for the finest mesh ran with polynomial order $p = 3$.

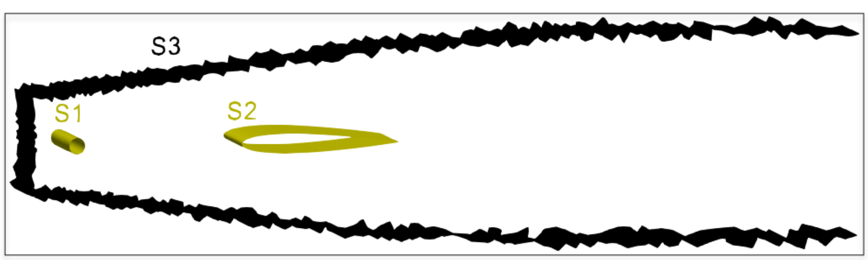

Fig. 8 FWH and solid and porous surface geometries. Solid surfaces are denoted s1 and s2 and the porous surface is s3.

The farfield acoustics are computed using two FWH surfaces, a solid surface that consists of the rod and airfoil walls and a porous surface as shown in Fig. 8. The porous surface takes a c-like shape and starts from 0.3C in front of the rod and up to 4C behind the airfoil as shown. This porous surface is chosen as to enclose all the relevant turbulent structures in the near-field region as shown in Fig. 9.

The results of the power spectral density (PSD) using the FWH solver are computed for three farfield observers as presented in Fig. 10. The location of these observers is calculated in the mid-plane based on an origin at half the airfoil chord and a distance R = 18.5C. These points are at three different angles measured from the trailing edge of the airfoil.

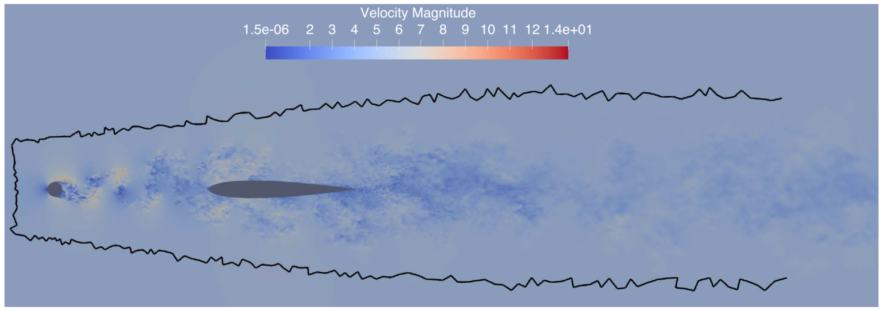

Fig. 9 FWH porous surface extent and geometry with respect to relevant flow structures and vortex shedding in the wake. Flow structures are represented by the velocity magnitude field.

For the first observer located at an angle $\theta = 60^o$ which is towards the downstream of the airfoil, we can see that the PyFR results match quite well with the experimental data of Jacob [22] for both the solid and porous surfaces. For the porous surface, both the tonal peak frequency and peak levels of PyFR have an almost perfect agreement with Jacob's experiment [22]. For the solid surface, while the peak frequency matches well with the experiments, the peak level is slightly lower than both the LES data of Giret and experimental data. However, compared to Giret's LES results for the solid surface, the peak tonal frequency of PyFR's LES data matches better with that of Jacob's experiment.

Coming to the second observer at $\theta = 90^o$, PyFR results for the porous surface show good agreement to experimental data. There is slight underprediction of the peak level, although it is still significantly better than other LES studies of Giret et. al [20] and Eltaweel and Wang [19], where in the latter they employed a hybrid LES-BEM using boundary element (BEM) solution for the Lighthill acoustic analogy [53]. In addition, Eltaweel and Wang's data [19] does not match with the peak tonal frequency predicted by the reference experiment [22]. For the solid surface, PyFR has lower peak levels compared to the experiment but matches well with the peak tonal frequency predicted by the experiment.

The 3$^{\text{rd}}$ observer is located at an angle of $\theta = 120°$. For the porous case, both Giret et. al's LES [20] and PyFR slightly underpredict the peak level compared to the experiments but have good agreement with regard to peak frequency. For the solid surface, PyFR matches the experimental peak tonal frequency quite well compared to reference LES data, although the peak level is slightly underpredicted.

In general the acoustic results show very good agreement in predicting the tonal peak as well as the broadband spectrum despite small under prediction of tonal peak values at some observer locations. In addition, it can be seen that the porous surface results usually have higher PSD levels for the low frequency region. This can be attributed to the lack of enough mesh refinement at the FWH surface or that it may need to be a tighter surface to increase its level of accuracy. A study of the best surface location can help reduce these PSD levels at low frequencies. Moreover, it is worth noting that the lack of enough smoothing at high frequencies is related to the use of spline fitting to fit the time history of flow variables sampled on the FWH surface and re-sample them at uniform time-steps since PyFR uses adaptive time-stepping with non-uniform time-steps. This sometimes introduces some artificial waves at very high frequencies, however, their amplitudes remain bounded as can be seen from the figures. It is also expected that increasing the number of windows used to converge the acoustics data can reduce these oscillations.

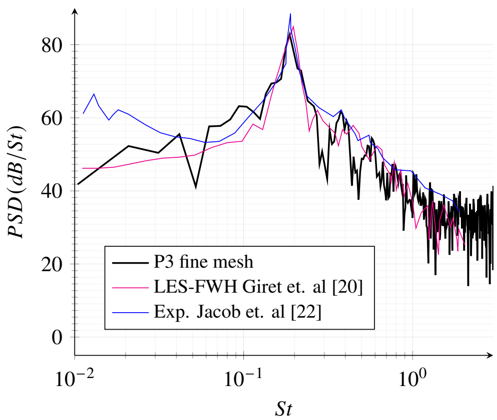

(a) 60^o, solid surface

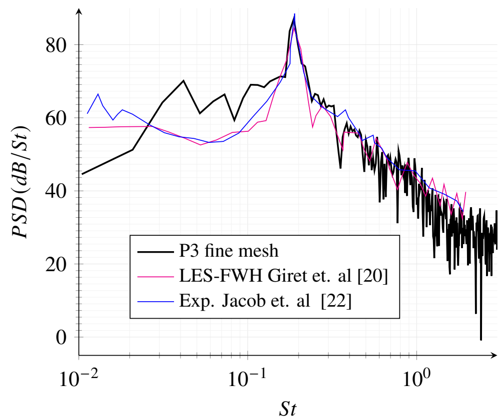

(b) 60^o, porous surface

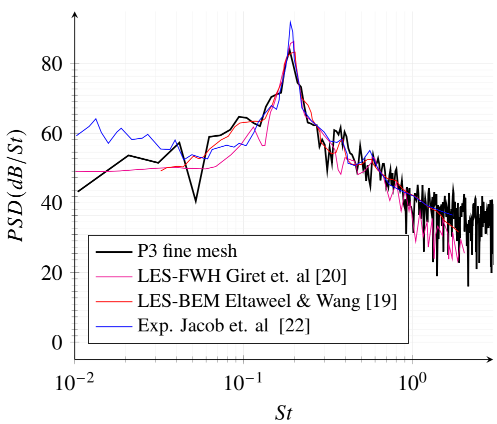

(c) 90^o, solid surface

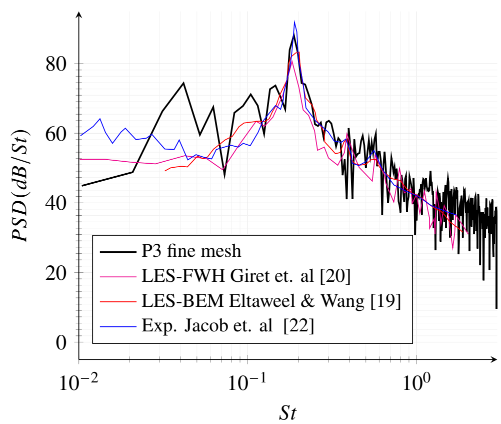

(d) 90^o, porous surface

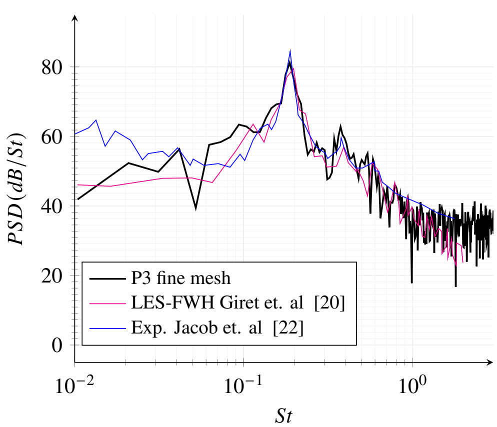

(e) 120^o, solid surface

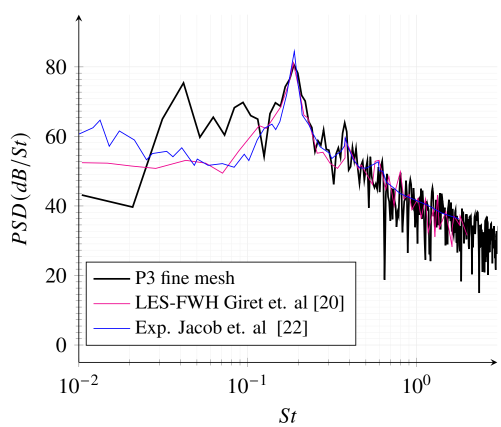

(f) 120^o, porous surface

Fig. 10 Comparison of farfield acoustics at a distance R = 18.5C measured from half chord and $\theta = 60^o, 90^o, 120^o$ measured from the airfoil T.E.

V. Conclusions and Future work

In this paper, we presented acoustic prediction results using the high-order FR method with polynomial order $p = 3$ for the airfoil-rod benchmark case in a hybrid LES-FWH approach. The results were in very good agreement with the literature despite some differences in the turbulent statistics and the tonal noise peak values. In general, the solid FWH surface shown better overall agreement with the literature especially for the low frequency regions compared to the porous surface results. On the other hand, porous surface results for the tonal peak matched the experimental results better than other LES-FWH and LES-BEM results in the literature. Three meshes were employed in the simulations with varying first cell heights on the rod surface resulting in different y^+ values while keeping both x^+ and z^+ unchanged. From these results it can be seen that changes in the y^+ did not affect the turbulent statistics much and this indicates that refinement in the z^+ direction may be required to achieve better agreement with the experiments in addition to longer averaging time for the turbulent statistics. Future work will include a more consistent mesh and order refinement in order to better converge the aerodynamic and turbulent statistics results.

References

[1] Liu, J., Kailasanath, K., Ramamurti, R., Munday, D., Gutmark, E., and Lohner, R., "Large-Eddy Simulations of a Supersonic Jet and Its Near-Field Acoustic Properties," *AIAA J.*, Vol. 47, No. 8, 2009, pp. 1849–1865. https://doi.org/10.2514/1.43281.

[2] Mendez, S., Shoeybi, M., Lele, S. K., and Moin, P., "On the Use of the Ffowcs Williams-Hawkings Equation to Predict Far-Field Jet Noise from Large-Eddy Simulations," *International Journal of Aeroacoustics*, Vol. 12, No. 1/2, 2013, pp. 1–20.

[3] Brès, G. A., Ham, F. E., Nichols, J. W., and Lele, S. K., "Unstructured Large-Eddy Simulations of Supersonic Jets," *AIAA Journal*, Vol. 55, No. 4, 2017, pp. 1164–1184. https://doi.org/10.2514/1.J055084.

[4] Liu, J., Corrigan, A. T., Kailasanath, K., Ramamurti, R., and Gutmark, E. J., "Helical Screech Tone Generation in an Overexpanded Jet," *23rd AIAA/CEAS Aeroacoustics Conference*, American Institute of Aeronautics and Astronautics, Denver, Colorado, 2017. https://doi.org/10.2514/6.2017-3208.

[5] Lyrintzis, A. S., and Coderoni, M., "The Use of Large Eddy Simulations in Jet Aeroacoustics," *AIAA Scitech 2019 Forum*, American Institute of Aeronautics and Astronautics, 2019. https://doi.org/10.2514/6.2019-0633.

[6] Casalino, D., Jacob, M., and Roger, M., "Prediction of Rod-Airfoil Interaction Noise Using the Ffowcs-Williams-Hawkings Analogy," *AIAA J.*, Vol. 41, No. 2, 2003, pp. 182–191. https://doi.org/10.2514/2.1959.

[7] Greschner, B., Thiele, F., Jacob, M. C., and Casalino, D., "Prediction of Sound Generated by a Rod–Airfoil Configuration Using EASM DES and the Generalised Lighthill/FW-H Analogy," *Computers & Fluids*, Vol. 37, No. 4, 2008, pp. 402–413. https://doi.org/10.1016/j.compfluid.2007.02.013.

[8] Caraeni, M., Aybay, O., and Holst, S., "Tandem Cylinder and Idealized Side Mirror Far-Field Noise Predictions Using DES and An Efficient Implementation of FW-H Equation," *17th AIAA/CEAS Aeroacoustics Conference (32nd AIAA Aeroacoustics Conference)*, American Institute of Aeronautics and Astronautics, 2011. https://doi.org/10.2514/6.2011-2843.

[9] Zhang, Y., Chen, H., Wang, K., and Wang, M., "Aeroacoustic Prediction of a Multi-Element Airfoil Using Wall-Modeled Large-Eddy Simulation," *AIAA J.*, Vol. 55, No. 12, 2017, pp. 4219–4233. https://doi.org/10.2514/1.J055853.

[10] Huynh, H. T., "A Flux Reconstruction Approach to High-Order Schemes Including Discontinuous Galerkin Methods," *18th AIAA Computational Fluid Dynamics Conference*, American Institute of Aeronautics and Astronautics, 2007. https://doi.org/10.2514/6.2007-4079.

[11] Wang, Z. J., Gao, H., and Haga, T., "A Unifying Discontinuous Formulation for Hybrid Meshes," *Adaptive High-Order Methods in Computational Fluid Dynamics*, World Scientific, 2011, pp. 423–453.

[12] Alhawwary, M., and Wang, Z. J., "Fourier Analysis and Evaluation of DG, FD and Compact Difference Methods for Conservation Laws," *J. Comput. Phys.*, Vol. 373, 2018, pp. 835–862. https://doi.org/10.1016/j.jcp.2018.07.018.

[13] Alhawwary, M. A., and Wang, Z. J., "Comparative Fourier Analysis of DG, FD and Compact Difference Schemes," *2018 Fluid Dynamics Conference, AIAA Aviation Forum*, AIAA-2018-4267, Atlanta, GA, 2018. https://doi.org/10.2514/6.2018-4267.

[14] Vermeire, B., and Vincent, P., "On the Properties of Energy Stable Flux Reconstruction Schemes for Implicit Large Eddy Simulation," *J. Comput. Phys.*, Vol. 327, 2016, pp. 368–388. https://doi.org/10.1016/j.jcp.2016.09.034.

[15] Wang, Z. J., Li, Y., Jia, F., Laskowski, G. M., Kopriva, J., Paliath, U., and Bhaskaran, R., "Towards Industrial Large Eddy Simulation Using the FR/CPR Method," *Comput. Fluids*, Vol. 156, 2017, pp. 579–589. https://doi.org/10.1016/j.compfluid.2017.04.026.

[16] Alhawwary, M., and Wang, Z., "On the Mesh Resolution of Industrial LES Based on the DNS of Flow over the T106C Turbine," *Adv. Aerodyn.*, Vol. 1, No. 1, 2019, p. 21. https://doi.org/10.1186/s42774-019-0023-6.

[17] Boudet, J., Casalino, D., Jacob, M., and Ferrand, P., "Prediction of Broadband Noise: Airfoil in the Wake of a Rod," *42nd AIAA Aerospace Sciences Meeting and Exhibit*, American Institute of Aeronautics and Astronautics, 2004. https://doi.org/10.2514/6.2004-852.

[18] Caraeni, M., Dai, Y., and Caraeni, D., "Acoustic Investigation of Rod Airfoil Configuration with DES and FWH," *37th AIAA Fluid Dynamics Conference and Exhibit*, Fluid Dynamics and Co-located Conferences, American Institute of Aeronautics and Astronautics, 2007. https://doi.org/10.2514/6.2007-4106.

[19] ELTaweel, A., and Wang, M., "Numerical Simulation of Broadband Noise from Airfoil-Wake Interaction," *17th AIAA/CEAS Aeroacoustics Conference (32nd AIAA Aeroacoustics Conference)*, American Institute of Aeronautics and Astronautics, 2011. https://doi.org/10.2514/6.2011-2802.

[20] Giret, J.-C., Sengissen, A., Moreau, S., Sanjosé, M., and Jouhaud, J.-C., "Noise Source Analysis of a Rod–Airfoil Configuration Using Unstructured Large-Eddy Simulation," *AIAA J.*, Vol. 53, No. 4, 2015, pp. 1062–1077. https://doi.org/10.2514/1.J053371.

[21] Jin, Y., Liao, F., Cai, J., and Morris, P. J., "Investigation on Rod-Airfoil Noise with High-Order Cell-Centered Finite Difference Method and Acoustic Analogy," *Aerospace Science and Technology*, Vol. 102, 2020, p. 105851. https://doi.org/10.1016/j.ast.2020.105851.

[22] Jacob, M. C., Boudet, J., Casalino, D., and Michard, M., "A Rod-Airfoil Experiment as a Benchmark for Broadband Noise Modeling," *Theor. Comput. Fluid Dyn.*, Vol. 19, No. 3, 2005, pp. 171–196. https://doi.org/10.1007/s00162-004-0108-6.

[23] Casalino, D., and Jacob, M., "Prediction of Aerodynamic Sound from Circular Rods via Spanwise Statistical Modelling," *Journal of Sound and Vibration*, Vol. 262, No. 4, 2003, pp. 815–844. https://doi.org/10.1016/S0022-460X(02)01136-7.

[24] Witherden, F., Farrington, A., and Vincent, P., "PyFR: An open source framework for solving advection–diffusion type problems on streaming architectures using the flux reconstruction approach," *Computer Physics Communications*, Vol. 185, No. 11, 2014, pp. 3028–3040. https://doi.org/10.1016/j.cpc.2014.07.011.

[25] Witherden, F., Vermeire, B., and Vincent, P., "Heterogeneous computing on mixed unstructured grids with PyFR," *Computers & Fluids*, Vol. 120, 2015, pp. 173–186. https://doi.org/10.1016/j.compfluid.2015.07.016.

[26] Vincent, P. E., Castonguay, P., and Jameson, A., "A New Class of High-Order Energy Stable Flux Reconstruction Schemes," *J. Sci. Comput.*, Vol. 47, No. 1, 2011, pp. 50–72. https://doi.org/10.1007/s10915-010-9420-z.

[27] Castonguay, P., Williams, D. M., Vincent, P. E., and Jameson, A., "Energy Stable Flux Reconstruction Schemes for Advection–Diffusion Problems," *Comput. Methods Appl. Mech. Eng.*, Vol. 267, 2013, pp. 400–417. https://doi.org/10.1016/j.cma.2013.08.012.

[28] Gao, H., Wang, Z. J., and Huynh, H. T., "Differential Formulation of Discontinuous Galerkin and Related Methods for the Navier-Stokes Equations," *Commun. Comput. Phys.*, Vol. 13, No. 04, 2013, pp. 1013–1044. https://doi.org/10.4208/cicp.020611.090312a.

[29] Wang, Z., and Gao, H., "A unifying lifting collocation penalty formulation including the discontinuous Galerkin, spectral volume/difference methods for conservation laws on mixed grids," *Journal of Computational Physics*, Vol. 228, No. 21, 2009, pp. 8161–8186. https://doi.org/https://doi.org/10.1016/j.jcp.2009.07.036.

[30] Crabill, J., Witherden, F., and Jameson, A., "A parallel direct cut algorithm for high-order overset methods with application to a spinning golf ball," *Journal of Computational Physics*, Vol. 374, 2018, pp. 692–723. https://doi.org/https://doi.org/10.1016/j.jcp.2018.05.036.

[31] Alhawwary, M. A., and Wang, Z. J., "DNS and LES of the flow over the T106C turbine using the high-order FR/CPR method," *AIAA Scitech 2020 Forum*, American Institute of Aeronautics and Astronautics, AIAA-2020-1572, 2020. https://doi.org/10.2514/6.2020-1572.

[32] Iyer, A., Abe, Y., Vermeire, B., Bechlars, P., Baier, R., Jameson, A., Witherden, F., and Vincent, P., "High-order accurate direct numerical simulation of flow over a MTU-T161 low pressure turbine blade," *Computers & Fluids*, Vol. 226, 2021, p. 104989. https://doi.org/https://doi.org/10.1016/j.compfluid.2021.104989.

[33] Dzanic, T., Girimaji, S., and Witherden, F., "Partially-averaged Navier–Stokes simulations of turbulence within a high-order flux reconstruction framework," *Journal of Computational Physics*, Vol. 456, 2022, p. 110992. https://doi.org/https://doi.org/10.1016/j.jcp.2022.110992.

[34] Huynh, H. T., Wang, Z. J., and Vincent, P. E., "High-Order Methods for Computational Fluid Dynamics: A Brief Review of Compact Differential Formulations on Unstructured Grids," *Comput. Fluids*, Vol. 98, 2014, pp. 209–220. https://doi.org/10.1016/j.compfluid.2013.12.007.

[35] Witherden, F., Vincent, P., and Jameson, A., "High-Order Flux Reconstruction Schemes," *Handbook of Numerical Analysis*, Vol. 17, Elsevier, 2016, pp. 227–263. https://doi.org/10.1016/bs.hna.2016.09.010.

[36] Rusanov, V., "The calculation of the interaction of non-stationary shock waves and obstacles," *USSR Computational Mathematics and Mathematical Physics*, Vol. 1, No. 2, 1962, p. 304–320. https://doi.org/10.1016/0041-5553(62)90062-9.

[37] Cockburn, B., and Shu, C.-W., "The Local Discontinuous Galerkin Method for Time-Dependent Convection-Diffusion Systems," *SIAM J. Numer. Anal.*, Vol. 35, No. 6, 1998, pp. 2440–2463.

[38] Kennedy, C. A., Carpenter, M. H., and Lewis, R., "Low-storage, explicit Runge–Kutta schemes for the compressible Navier–Stokes equations," *Applied Numerical Mathematics*, Vol. 35, No. 3, 2000, pp. 177–219. https://doi.org/10.1016/s0168-9274(99)00141-5.

[39] Williams, J. E. F., and Hawkings, D. L., "Sound Generation by Turbulence and Surfaces in Arbitrary Motion," *Philos. Trans. R. Soc. Lond. Ser. Math. Phys. Sci.*, Vol. 264, No. 1151, 1969, pp. 321–342.

[40] di Francescantonio, P., "A NEW BOUNDARY INTEGRAL FORMULATION FOR THE PREDICTION OF SOUND RADIATION," *Journal of Sound and Vibration*, Vol. 202, No. 4, 1997, pp. 491–509. https://doi.org/10.1006/jsvi.1996.0843.

[41] Lockard, D. P., "AN EFFICIENT, TWO-DIMENSIONAL IMPLEMENTATION OF THE FFOWCS WILLIAMS AND HAWKINGS EQUATION," *Journal of Sound and Vibration*, Vol. 229, No. 4, 2000, pp. 897–911. https://doi.org/10.1006/jsvi.1999.2522.

[42] Ghorbaniasl, G., and Lacor, C., "A Moving Medium Formulation for Prediction of Propeller Noise at Incidence," *Journal of Sound and Vibration*, Vol. 331, No. 1, 2012, pp. 117–137. https://doi.org/10.1016/j.jsv.2011.08.018.

[43] Farassat, F., "Derivation of Formulations 1 and 1A of Farassat," Tech. rep., Mar. 2007.

[44] Lockard, D., "A Comparison of Ffowcs Williams-Hawkings Solvers for Airframe Noise Applications," *8th AIAA/CEAS Aeroacoustics Conference & Exhibit*, American Institute of Aeronautics and Astronautics, 2002. https://doi.org/10.2514/6.2002-2580.

[45] Najafi-Yazdi, A., Brès, G. A., and Mongeau, L., "An Acoustic Analogy Formulation for Moving Sources in Uniformly Moving Media," *Proc. R. Soc. Lond. Math. Phys. Eng. Sci.*, 2010, p. rspa20100172. https://doi.org/10.1098/rspa.2010.0172.

[46] Ghorbaniasl, G., Huang, Z., Siozos-Rousoulis, L., and Lacor, C., "Analytical Acoustic Pressure Gradient Prediction for Moving Medium Problems," *Proc. R. Soc. A*, Vol. 471, No. 2184, 2015, p. 20150342. https://doi.org/10.1098/rspa.2015.0342.

[47] Alhawwary, M. A., and Wang, Z. J., "Implementation of a FWH Approach in a High-Order LES Tool for Aeroacoustic Noise Predictions," *AIAA Scitech 2020 Forum*, AIAA 2020-1724, 2020. https://doi.org/10.2514/6.2020-1724.

[48] Eltaweel, A., Wang, M., Kim, D., Thomas, F. O., and Kozlov, A. V., "Numerical Investigation of Tandem-Cylinder Noise Reduction Using Plasma-Based Flow Control," *J. Fluid Mech.*, Vol. 756, 2014, pp. 422–451. https://doi.org/10.1017/jfm.2014.420.

[49] Achenbach, E., "Distribution of local pressure and skin friction around a circular cylinder in cross-flow up to Re = 5 × 106," *Journal of Fluid Mechanics*, Vol. 34, No. 4, 1968, p. 625–639. https://doi.org/10.1017/S0022112068002120.

[50] Boudet, J., "Approches Numériques Pour la Simulation du Bruit à Large Bande en vue de L'application aux Turbomachines," Ph.D. thesis, École Centrale de Lyon, 2003.

[51] Szepessy, S., and Bearman, P. W., "Aspect ratio and end plate effects on vortex shedding from a circular cylinder," *Journal of Fluid Mechanics*, Vol. 234, 1992, p. 191–217. https://doi.org/10.1017/S0022112092000752.

[52] Welch, P., "The Use of Fast Fourier Transform for the Estimation of Power Spectra: A Method Based on Time Averaging over Short, Modified Periodograms," *IEEE Trans. Audio Electroacoustics*, Vol. 15, No. 2, 1967, pp. 70–73. https://doi.org/10.1109/TAU.1967.1161901.

[53] Lighthill, M. J., "On Sound Generated Aerodynamically. II. Turbulence as a Source of Sound," *Proc. R. Soc. Lond. Ser. Math. Phys. Sci.*, Vol. 222, No. 1148, 1954, pp. 1–32.